RSC Advances

ROYAL SOCIETY OF CHEMISTRY

www.rsc.org/advances

$LiMn_2O_4$/Graphene composites as cathode with enhanced electrochemical performance for lithium-ion capacitors

Jing Li [a, b,*], Xia Zhang [a, b,*], Rufang Peng [a, b], Yeju Huang [c], Lei Guo [a, b], Yongcheng Qi [a, b]

[a]*School of Materials Science and Engineering, Southwest University of Science and Technology, Mianyang 621010, China*

[b]*State Key Laboratory Cultivation Base for Nonmetal Composites and Functional Materials, Southwest University of Science and Technology, Mianyang 621010, China*

[c]*School of National Defence Science and Technology, Southwest University of Science and Technology, Mianyang 621010, China*

*Corresponding author. Tel.: +86-15983676338; fax: + 86-816-2419011.

E-mail address: xy13787103391@126.com (J. Li), zyx02090229@163.com (X. Zhang)

Abstract

A $LiMn_2O_4$ microspheres (LMO-MSs)/graphene nanosheets (GNSs) composite has been synthesized using γ-MnO_2 microspheres as a precursor. It is characterized with X-ray diffraction (XRD), scanning electron microscope (SEM), transmission electron microscope (TEM) and energy dispersive spectrometer (EDS), et al. The test results suggest that the sphere-like LMO-MSs structures were successfully coated by the GNSs. A novel lithium-ion capacitor was fabricated using activated carbon as the anode electrode and LMO-MSs@GNSs composites as the cathode electrode. The electrochemical properties were investigated by galvanostatic charge/discharge cycling and cycling voltammetry. The electrochemical test results show that the energy density of LMO-MSs@GNSs composites lithium-ion capacitor presents 38.8 Wh kg^{-1} at power density 12.6 W kg^{-1} with organic electrolyte in the voltage range of 0-2.3 V. The synergistic effect of GNSs and LMO-MSs could significantly improve the electrical conductivity and provides more reaction sites, thereby resulting in better electrochemical properties for the composites. The high rate capacity and long stability make the LMO-MSs@GNSs composite as a electrode material for high-performance lithium-ion capacitors.

Keywords: $LiMn_2O_4$ microspheres; Graphene nanosheets; Lithium-ion Capacitor; Electrochemical property;

1. Introduction

The fast development of global economy is usually accompanied by a tremendous consumption of energy. The traditional energy, such as coal, fossil oil, gas, will be exhausted unavoidably in the near future. Therefore, it is urge and important to develop devices for new energy storage and conversion.[1-3] Supercapacitor is such an important energy storage device that can bridge the power/energy gap between traditional dielectric capacitors and regular batteries/fuel cells.[4-7] It has received a considerable attention because of the outstanding properties, such as a high power density, a long cycle life and rapid charge-discharge rates.[8] But one of the drawbacks of the commercial supercapacitors based on carbon electrodes is a low energy density, the fact which hindering the large-scale application of supercapacitors.[9-11] Up to now, many efforts have been made to increase the energy density of supercapcitors without sacrificing their power capacity. Apart from increasing the specific capacitance of electrodes, an attractive approach is to develop lithium-ion capacitors,[12, 13] which can increase the operating voltage window by using two different electrodes, resulting in a considerable energy density.[14] Regarding the combination of the advantages of both battery electrodes and capacitor electrodes, lithium-ion capacitors will be one of the most promising energy storage devices. So far, various lithium-ion capacitor systems, such as aqueous $LiMn_2O_4$ nanohybrid/AC system at a voltage of 1.8 V with its energy density of 29.8 $Wh \cdot kg^{-1}$ at power density of 90 $W \cdot kg^{-1}$,[15] aqueous $LiMn_2O_4$/AC system at a voltage of 1.8 V with its energy density of 35.0 $Wh \cdot kg^{-1}$.[16] However, the seeking for new electrode materials with lower cost and better properties is still very

important in the development of lithium-ion capacitors.

As a cathode material, $LiMn_2O_4$ with a spinel structure is one of the most promising cathode materials because they are inexpensive and safe.[17] However, there are still several challenges that need to be overcome, such as low electronic conductivity and the dissolution of manganese.[18-20] To address these issues, many strategies, such as new preparation methods,[21-23] doping techniques [24-26] and surface modifications,[27, 28] have been developed for the synthesis of $LiMn_2O_4$ with high performance. Furthermore, it has been reported that nanostructured $LiMn_2O_4$, such as nanoparticles,[29] nanowires,[30] nanorods,[31] nanotubes[32] and nanochain,[33] can present good electrochemical performance. The reduced particle size of $LiMn_2O_4$ can facilitate the transportation of lithium ions and electrons during cycling. Recently, graphene, as a kind of new carbon material, has aroused special attention due to its two-dimensional nanostructure.[34] This unique nano-structure holds great potential because of its excellent electronic conductivity, large surface area (2600 $m^2 \cdot g^{-1}$) and good mechanical flexibility. [35]

Herein, we demonstrate a facile and green synthesis without the application of any surfactant or template to synthesize $LiMn_2O_4$ microspheres/graphene nanosheets (LMO-MSs@GNSs) composite as a high-performance electrode material for lithium-ion capacitors. The grain morphology of $LiMn_2O_4$ shows a sphere-like appearance with numerous well-arranged nanoparticles. The GNSs are coated on the sphere-like surface of LMO-MSs. We have designed and fabricated a novel lithium-ion capacitors using LMO-MSs@GNSs composites and activated carbon (AC)

electrodes as cathode and anode, respectively. The LMO-MSs@GNSs composite is expected to exhibit high rate capability and long cycle stability because of its high surface area and good electronic conductivity attributed to GNSs. The obtained results of the composites suggest a promising application as a good supercapacitor electrode material with high performances.

2. Experimental

Nature flake graphite (NG, ≦30 μm) was purchased from Shanghai Huayi Group. Lithium manganate (LMO, ≦200 nm) was purchased from Shandong Yiwei Group. Sodium nitrate ($NaNO_3$, 99%), sulfuric acid (H_2SO_4, 98%), potassium permanganate ($KMnO_4$, 99.5%), hydrogen peroxide (H_2O_2, 30%), hydrochloric acid (HCl, 5%), manganese sulfate ($MnSO_4 \cdot H_2O$, 99%), sodium peroxydisulfate ($Na_2S_2O_8$, 99.0%) and lithium hydroxide monohydrate ($LiOH \cdot H_2O$, 99.0%) were purchased from Chengdu Kelong Chemicals Company. All reagents used were of analytical grade without further purification. The deionized water with resistivity of 18.2 MΩ·cm was prepared by a Millipore Milli-Q UF plus lab ultra pure water purification system, and used as the solvent in all experiments.

2.1. Material preparation

Graphene oxide (GO) was fabricated from NG by the modified Hummers' method.[36] In a typical experiment GO, 1.0 g NG and 0.5 g $NaNO_3$ were mixed with 46 mL H_2SO_4 for 15 min. 3.0 g of $KMnO_4$ was then slowly added into the above solution under strong stirring with keeping the temperature constant at bellow 10 ℃ for 2 h in an ice bath. Subsequently, the solution was kept at 38 °C for 15 h.

Afterwards, 90 mL of deionized water was dropped slowly into the solution and the resultant solution was kept at 95 °C for 15 min. The remaining $KMnO_4$ and impurities in the solution after reaction were removed by adding 15 mL of H_2O_2, 250mL HCl and deionized water, successively. The GO solution was ultrasoniced for 6 h. The resulted pure GO was washed with deionized water, centrifuged, and freeze-dried for 24 h.

The synthesis of LMO-MSs was carried out through a two-step procedure. Firstly, the γ-MnO_2 microspheres were successfully synthesized through a simple, low-cost and eco-friendly green process. 5.07 g $MnSO_4 \cdot H_2O$ and 7.14 g $Na_2S_2O_8$ were dissolved in 20 mL of deionized water, respectively. The mixed aqueous solution was kept undisturbed at 50 ^oC for 24 h. A black deposition was then formed at the bottom of the container. After washing with deionized water, filtrating through micro-porous membrane and freeze-dried, the target γ-MnO_2 spheres were finally obtained. The as prepared γ-MnO_2 and $LiOH \cdot H_2O$ were mixed at a molar ratio of 2:1.05, and the mixture was grounded with ethanol to obtain a superfine mixture. After evaporation of ethanol, the mixture was collected into an alumina crucible for sintering under an air atmosphere with the temperature controlled from room temperature to 750 ^oC and a heating rate of 10 ^oC/min. The mixture was kept at 500 ^oC for 4 h and then 750 ^oC for 10 h in air to obtain spinel LMO-MSs. The GNSs were prepared with 2 $g \cdot L^{-1}$ 100 mL GO solution by hydrothermal reduction at 100 °C for 24 h. The 0.5 g LMO-MSs was added to 100 mL GNSs solution with vigorous string at 25 ^oC for 5 h. The obtained LMO-MSs@GNSs composites were washed with deionized water, centrifuged, and

freeze-dried for 24 h.

2.2. Material characterization

The crystal structure of the materials was determined by a powder X-ray diffractometer (PANalytical, X'Pert PRO) using Cu-Kα radiation at 40 kV and 40 mA, $2\theta = 3 \sim 80^{o}$, acquisition time of 10 s per spot. The morphology, microstructure were investigated by a field emission scanning electron microscope (FESEM, Ultra-55) and transmission electron microscope (TEM, Libra200FE). The elemental mapping were obtained on an Oxford IETEM100 energy dispersive spectrometer of the Libra200FE transmission electron microscope. The elemental composition was determined by energy dispersive spectroscopy (EDS) measurements using an Oxford IE450X-Max80 EDX spectrometer, an accessory of field emission scanning electron microscope, operated at 15 kV, with spot size of 2 nm and acquisition time of 40 s per spot. The content of Mn ions in the electrolyte was investigated by inductively coupled plasma emission spectrometer (ICP-AES, Thermo iCAP6500), operated at power of 1150 w, pump speed of 50 rpm, auxiliary gas flow of 0.5 $L \cdot min^{-1}$, nebulizer gas flow of 0.55 $L \cdot min^{-1}$, cooling gas flow of 12 $L \cdot min^{-1}$.

2.3. Electrochemical measurement

The electrochemical measurements were tested by CR2016 coin-type cells with active carbon as anode electrode and synthesized products as cathode electrode. The cathode electrodes consist of 75 wt.% synthesized product, 15 wt.% carbon black as conductive agent, and 10 wt.% of polyvinylidene fluoride (PVDF) as binder dissolved in N-methyl-2-pyrrolidone (NMP). The anode electrode contains 86 wt.% activated

carbon (AC, YP-50), 6 wt.% Super P and 8 wt.% PVDF. The current collectors for cathode and anode electrodes were 20-μm-thick aluminum foil .After the coating procedure, the resulting two types of electrodes were compressed to round cathode plates (average diameter 15 mm), pressed and dried at 80 ^{o}C for 24 h. The separator was Celgard2400 polypropylene membrane. The electrolyte was 1 M $LiPF_6$ in ethylene carbonate (EC)/diethyl carbonate (DEC)/dimethyl carbonate (DMC) (1:1:1, in vol%). The LMO/AC, LMO-MSs/AC and LMO-MSs@GNSs/AC lithium-ion capacitors of (m_+/m_-)= 0.65 were assembled in the glove box filled with argon gas (MBRAUN, H_2O<0.1 ppm, O_2<0.1 ppm). The galvanostatic charge-discharge tests (GC) were investigated by a LAND CT2001A battery testing system. The cyclic voltammetry (CV) measurements were conducted on a electrochemical workstation (ChI660E). The electrochemical impedance spectroscopy (EIS) measurements were performed with a electrochemical workstation (ChI660E) with 5 mV amplitude in a frequency range from 1 MHz to 0.01 Hz at open circuit potential. The specific capacity, energy densities and power densities in the full-cell devices were calculated according to the equations:[37, 38]

$$C = It / \Delta U m \quad (1)$$

$$E = \int U dC = I \int U dt/m \quad (2)$$

$$P = U_m I / m \quad (3)$$

where C denotes the specific capacitance of a full cell, E is the energy density ($Wh \cdot kg^{-1}$) and P is the power density ($W \cdot kg^{-1}$), I denotes the discharge current (A), t refers to the total discharge time (s), m is the weight of total active materials in both

cathode and anode (g), ΔU is the potential drop during discharge (V), U is the cell voltage (V) and Um is the average discharge voltage (V).

3. Results and discussion

3.1. Structure and morphology of γ-MnO_2, LMO, LMO-MSs and LMO-MSs@GNSs composites

To ascertain the crystal structure of the obtained products, X-ray diffraction (XRD) analysis was performed. The XRD patterns of as-prepared GNSs, γ-MnO_2, LMO, LMO-MSs and LMO-MSs@GNSs composites are displayed in Fig. 1. As can be seen, the precursor MnO_2 can be ascribed to γ-MnO_2 (JCPDS No. 24-0735).[39] The sharp and narrow diffraction peaks with no additional impurity phase indicate that the diffraction peaks of the LMO, LMO-MSs and LMO-MSs@GNSs composites index well to the spinel $LiMn_2O_4$ structure (JCPDS No. 35-0782) and no other impurity peaks are detected.[40] The flat base line and sharp main peaks indicate that all of samples are well crystallized. Diffraction peaks of LMO-MSs@GNSs are weaker and wider, which indicates that the GNSs were successfully coated on the surface of LMO-MSs, the diffraction peaks still well match that of LMO.

To elucidate the morphology and microstructure of LMO-MSs@GNSs composites, SEM measurements were carried out. Fig. 2a-b, c-d and e-f shows the SEM images of γ-MnO_2, LMO-MSs and LMO-MSs@GNSs composites, respectively. γ-MnO_2 presents spherical morphology with the diameter of 3 - 7μm. From Fig. 2b, we can see that the surface of these spheres is self-assembled by large numbers of nanohorns. On the contrary, the SEM image of LMO-MSs (Fig. 2c-d) shows micro-spheres which

comprise nanoparticles. Fig. 2c shows that LMO-MSs keeps the precursor's morphology with a sphere diameter ranging from 4 to 8μm, while the cmmercial LMO particles are randomly stacked in Fig. 2g. The SEM images of LMO-MSs@GNSs composites (Fig. 2e-f) exhibits a similar morphology to that of LMO-MSs, revealing that sphere-like LMO-MSs structures are successfully coated by the GNSs. Further, Energy Dispersive Spectrometer (EDS) measurements demonstrate the existences of C, O, and Mn elements in the LMO-MSs@GNSs composites (Fig. 2h). The hollow structure and porous sphere provide possible channels which benefit the permeation of electrolyte into the inner of particles, resulting in excellent electrochemical performances.[28, 36]

To further identify the surface morphology of LMO-MSs and LMO-MSs@GNSs composites, TEM measurement was carried out. As seen in Fig. 3a and 3b, the LMO-MSs exhibit bald and smooth surface. However, the LMO-MSs@GNSs shows coarse surface and is covered by a nanofilm, which may be the multilayer GNSs. It manifests that the GNSs have been successfully coated and wrapped on the surface of LMO-MSs. Fig. 3c presents the HRTEM images of the LMO-MSs cathode materials. The regular lattice fringes suggest that the as-prepared pristine LMO-MSs are well crystallized. As seen in Fig. 3d, two distinguishable coating layers can be observed on the surface of LMO-MSs. It suggests that graphene nanosheets have be coated on the surface of the spherical LMO-MSs. Moreover, the ordered graphite lattices (circled by red line in Fig. 3d) are visible and the disordered regions are also found. It indicates that the graphene nanosheets are partially restored the ordered crystal structure of

LMO-MSs. The distribution of elements in the LMO-MSs@GNSs composite was also characterized by TEM and X-ray elemental mapping images (Figure 3e). These images reveal that carbon, oxygen, and manganese are uniformly distributed in the LMO-MSs@GNSs composites.

3.2 Electrochemical performance of LMO/AC, LMO-MSs/AC and LMO-MSs@GNSs /AC lithium-ion capacitors

The cyclic voltammetry (CV) is well known as an effective tool to investigate the capacitive behavior of a material. Fig. 4 shows the CV curves of the three samples between 0 V and 2.3 V at 10 $mV \cdot s^{-1}$. In Fig. 4, the CV curves of three electrodes have rectangular shape indicating of the capacitive behavior. The electrodes represent the absence of cathodic and anodic peaks. This suggests that no redox reaction occurs between AC and Li ions. Therefore, the non-faradic adsorption/desorption reaction of Li ions on the surface of AC makes the major contribution of the cell capacitance. The larger area of CV implies the higher specific capacitance of the electrode materials at the same scan rate.[5] Therefore, the specific capacitance of LMO-MSs@GNSs composites is higher than that of LMO and LMO-MSs as electrode materials of lithium-ion capacitor. The enhanced specific capacitance of LMO-MSs@GNSs composites might be ascribed to the increased electronic conductivity through GNSs on the surface of LMO-MSs.

Furthermore, the electrochemical performance was investigated using galvanostatic charge/discharge (GC) measurements. The GC curves of LMO/AC, LMO-MSs/AC and LMO-MSs@GNSs/AC lithium-ion capacitors at the current density of 2 C are

shown in Fig. 5. The specific capacitances of the electrodes were calculated according to Eq (1). The obtained charge/discharge curves are nearly linear and symmetric, revealing a good capacitive behavior. In addition, the voltage drop is observed to be very small, which indicates that these electrodes have low internal resistance. At a discharge current density of 2 C, the specific capacitance of LMO/AC, LMO-MSs/AC and LMO-MSs@GNSs/AC lithium-ion capacitor are 35.3, 35.5 and 43.7 $F \cdot g^{-1}$, respectively. This is mainly due to the well decoration of GNSs on the LMO-MSs and the outsanding structures of LMO-MSs, which reduce the dissolution of Mn ions for electrode and electrolyte accessibility.

To further explore the rate properties of LMO-MSs@GNSs composites, the charge/discharge curves are obtained at varying current densities, as displayed in Fig. 6. Fig. 6 shows the discharge curves of the three samples at rates of 0.5 C, 1 C, 2 C, 4 C, 8C, 10 C and 15 C. Obviously LMO-MSs@GNSs composites with sphere-like structure exhibit much higher specific capacity and rate capability. Interestingly, the initial capacity of LMO-MSs@GNSs composites reaches 53.2 $F \cdot g^{-1}$ at 0.5 C comparing to 41.9 $F \cdot g^{-1}$ at 0.5 C for LMO and LMO-MSs. At high rates of 4 C and 8 C, LMO-MSs@GNSs composites still possesses a specific capacity of 38.9 and 35.6 $F \cdot g^{-1}$, respectively, corresponding to a capacity retention rate of 73.1% and 66.9%, respectively, in comparison with 29.3 $F \cdot g^{-1}$, and 25.9 $F \cdot g^{-1}$ for specific capacity and 69.9% and 61.8% for retention rate, respectively, for LMO at the same discharge rates.

On the basis of the galvanostatic charge/discharge results, the energy density and

power density for LMO/AC, LMO-MSs/AC and LMO-MSs@GNSs/AC lithium-ion capacitors with same weight ratio were calculated according to Eq (2) and (3) and displayed by Ragone plots in Fig. 7 (gravimetric, on the base of the electrode mass). Fig. 7 presents power density as a function of energy density for a LMO-MSs@GNSs capacitor containing multilayer GNSs electrode with a uniform microstructure. The LMO-MSs@GNSs electrode has superior energy density even under high current density. The energy density of LMO-MSs@GNSs/AC capacitor reached 38.8 Wh kg^{-1} at a specific power density of 12.6 W kg^{-1} and was maintained at 23.6 Wh kg^{-1} even at a specific power density of 186.5 W kg^{-1}. Compared to LMO/AC capacitors, this energy density is about 1.73 times higher than those achieved by LMO-MSs@GNSs/AC lithium-ion capacitor at high rates of 10 C and 15 C (see Fig. 7). This remarkably improved energy and power density are assigned to good electronic conductivity attributed to GNSs, as well as their well designed microstructure [19, 28].

The cyclic stability of the as-prepared LMO/AC, LMO-MSs/AC and LMO-MSs@GNSs/AC lithium-ion capacitors was also measured by galvanostatic charge-discharge tests. Fig. 8 shows the specific capacity of the three samples within 500 cycles at 2 C. All materials show a certain capacity decay, which is dominated by the structure of $LiMn_2O_4$.[18, 22] The specific capacitance of LMO decreases gradually with increasing cycle numbers and its capacitance retention is only 56.9 % after 500 cycles. By contrast, LMO-MSs@GNSs composites only lost 9.4 % of its capacitance in the initial 500 cycles. As can be seen from Figure 8, the structure of LMO-MSs@GNSs composite is still kept in a spherical shape, and the sphere-like

structure of LMO-MSs@GNSs composite is not damaged in the process of preparing the electrode sheets. This indicates that the LMO-MSs@GNSs composite electrode has long-term electrochemical stability at such a current density. The content of Mn ions in the electrolyte for lithium-ion capacitors in Tab. 1. After cycling 500 times, the content of Mn ions of LMO-MSs@GNSs composite electrode in the electrolyte is only 0.265 ug·mL^{-1}. This result is attributed to the microstructure of LMO-MSs which may provide more active sites for charge-transfer reaction and reduce the dissolution of Mn ions in organic electrolyte. [37]

To further investigate the conductivity of the electrode materials. Electrochemical impedance spectroscopy (EIS) spectras were measured for the three materials after the 500th cycles at fully charged state (about 0.3 V). A possible equivalent circuit is provided as the inset of Fig. 9 for interpretation. R_e represents electrolyte ohmic resistance, while R_{sl} is the resistance for ions migration through the solid electrolyte interphase (SEI) film; C_{dl} and C_{sl} denote the double layer capacitance and passivation film capacitance, respectively. Z_w stands for the finite length Warburg impedance, and R_{ct} is the charge transfer resistance.[31, 37] It can be seen from Fig. 9 that the Nyquist plot of the three electrodes exhibits an almost vertical line in the low frequency region, and a small semicircle in the high frequency region. The diameter of the semicircle reflects the charge transfer resistance (R_{ct}), which concerns the diffusive resistance of ion diffusion into the electrode and the electrolyte into the interior of the electrode. The almost vertical line at low frequencies reveals the swift ion diffusion both in electrolyte and across the electrode surface, indicating a typical capacitive behavior of

the electrodes. The Re of LMO/AC, LMO-MSs/AC and LMO-MSs@GNSs/AC lithium-ion capacitors is 4.90, 2.42 and 3.55 Ω, respectively. The Rct of LMO/AC, LMO-MSs/AC and LMO-MSs@GNSs/AC lithium-ion capacitors is 15.5, 30.2 and 38.1 Ω, respectively. The Rct of LMO and LMO-MSs is sobviously larger than the capacitor containing the LMO-MSs@GNSs composites. Thus, we confirmed that the LMO-MSs@GNSs can facilitate the electrochemical reaction between the electrodes and Li ions during the charge-discharge process.

4. Conclusions

In summary, we have developed an effective route to synthesize LMO-MSs@GNSs composites by using microspheres γ-MnO_2 as precursor. The lithium-ion capacitors of as-synthesized LMO-MSs@GNSs composites as cathode show a specific capacity (53.2 $F \cdot g^{-1}$ at 0.5 C), excellent rate performances (38.9 and 35.6 $F \cdot g^{-1}$ for 4 C and 8 C), and lost 9.4 % of its capacitance in the initial 500 cycles at 2 C. This facile approach for preparation of LMO-MSs@GNSs composites provides us a new way to fabricate lithium manganate composites cathode materials with high-rate capability and long cycling stability due to the high surface area of the cathode nanoparticles and good electronic conductivity attributed to graphene. The present results suggest that the LMO-MSs@GNSs composite could be a promising electrode material for high-energy lithium-ion capacitors in view of the remarkably improved performance and moderate preparation method.

Acknowledgements

This work was financially supported by the National Natural Science Foundation of

China (No. 2013AA0509) and Postgraduate Innovation Fund of Southwest University of Science and Technology (No. 15ycx018).

References

1. W. Tang, L. Liu, S. Tian, L. Li, Y. Yue, Y. Wu and K. Zhu, *Chem. Commun.*, 2011, **47**, 10058-10060.
2. X. Wang, Y. Hou, Y. Zhu, Y. Wu and R. Holze, *Scientific reports*, 2013, **3**.
3. X. Du, C. Wang, M. Chen, Y. Jiao and J. Wang, *J. Phys. Chem. C*, 2009, **113**, 2643-2646.
4. A. Cultura II and Z. Salameh, *cell*, 2015, **1**, 1.
5. E. Jokar and S. Shahrokhian, *J. Solid State Electrochem.*, 2015, **19**, 269-274.
6. C. Lekakou, A. Sorniotti, C. Lei, F. Markoulidis, P. C. Wilson, A. Santucci, S. Tennison, N. Amini, C. Trapalis and G. Carotenuto, in *Electric Vehicle Batteries: Moving from Research towards Innovation*, Springer, 2015, pp. 33-43.
7. A. Jain, C. Xu, S. Jayaraman, R. Balasubramanian, J. Lee and M. Srinivasan, *Microporous Mesoporous Mater.*, 2015, **218**, 55-61.
8. C. Ramirez-Castro, O. Crosnier, L. Athouël, R. Retoux, D. Bélanger and T. Brousse, *J. Electrochem. Soc.*, 2015, **162**, A5179-A5184.
9. P. Simon, P.-L. Taberna and F. ois Béguin, *Edited by Francois Béguin and Elzbieta Fr şackowiak*, 2013.
10. L. Wei, M. Sevilla, A. B. Fuertes, R. Mokaya and G. Yushin, *Adv. Funct. Mater.*, 2012, **22**, 827-834.
11. T. Kim, G. Jung, S. Yoo, K. S. Suh and R. S. Ruoff, *ACS nano*, 2013, **7**, 6899-6905.
12. M. Liu, L. Zhang, P. Han, X. Han, H. Du, X. Yue, Z. Zhang, H. Zhang and G. Cui, *Particle & Particle Systems Characterization*, 2015, **32**, 1006-1011.
13. Y. K. Kwon, W. Choi, H.-S. Choi and J. K. Lee, *Electron. Mater. Lett.*, 2013, **9**, 751-754.
14. Z. Yang, Z. Mei, F. Xu, Y. Yao, W. Zhang, W. Qi, Q. Song, Z. Gao and T. Zhao, *J. Mater. Sci.*, 2013, **48**, 2512-2519.
15. F. Wang, S. Xiao, Y. Zhu, Z. Chang, C. Hu, Y. Wu and R. Holze, *J. Power Sources*, 2014, **246**, 19-23.
16. Y.-g. Wang and Y.-y. Xia, *Electrochem. Commun.*, 2005, **7**, 1138-1142.
17. D. Zhan, Q. Zhang, X. Hu, G. Zhu and T. Peng, *Solid State Ionics*, 2013, **239**, 8-14.
18. H. Zhao, F. Li, X. Liu, W. Xiong, B. Chen, H. Shao, D. Que, Z. Zhang and Y. Wu, *Electrochim. Acta*, 2015, **166**, 124-133.
19. M. H. Pyun and Y. J. Park, *J. Alloys Compd.*, 2015.
20. D. Cericola, P. Novák, A. Wokaun and R. Kötz, *Electrochim. Acta*, 2011, **56**, 8403-8411.
21. Q. Li, C. Peng, J. Huang, W. Xu, F. Yang, H. Bai, C. Su and J. Guo, *Int. J. Electrochem. Sci*, 2015, **10**, 7513-7520.
22. G. Liu, X. Kong, Y. Li and B. Wang, *Materials Technology: Advanced Performance Materials*, 2015, 1753555715Y. 0000000057.
23. X. Cao, G. Guo, F. Liu, Y. Zhou and S. Zhang, *Int. J. Electrochem. Sci*, 2015, **10**, 3841-3847.
24. Q. Liu, S. Wang, H. Tan, Z. Yang and J. Zeng, *Energies*, 2013, **6**, 1718-1730.

25. Y. Fu, H. Jiang, Y. Hu, Y. Dai, L. Zhang and C. Li, *Ind. Eng. Chem. Res.*, 2015, **54**, 3800-3805.
26. A. A. Uludag, A. Erdaş, Ş. Özcan, D. Nalci, M. O. Güler, T. Çetinkaya, M. Uysal and H. Akbulut, in *Progress in Clean Energy, Volume 2*, Springer, 2015, pp. 41-56.
27. H. Zhuo, S. Wan, C. He, Q. Zhang, C. Li, D. Gui, C. Zhu, H. Niu and J. Liu, *J. Power Sources*, 2014, **247**, 721-728.
28. K. Sreelakshmi, S. Sasi, A. Balakrishnan, N. Sivakumar, A. S. Nair, S. V. Nair and K. Subramanian, *Energy Technology*, 2014, **2**, 257-262.
29. D. Narsimulu, B. N. Rao, M. Venkateswarlu and N. Satyanarayana, *J. Indian Chem. Soc.*, 2015, **92**, 792-795.
30. S. Lee, Y. Oshima, E. Hosono, H. Zhou, K. Kim, H. M. Chang, R. Kanno and K. Takayanagi, *ACS nano*, 2014, **9**, 626-632.
31. B. N. Rao, P. Muralidharan, P. R. Kumar, M. Venkateswarlu and N. Satyanarayana, *Int. J. Electrochem. Sci*, 2014, **9**, 1207-1220.
32. W. Tang, Y. Hou, F. Wang, L. Liu, Y. Wu and K. Zhu, *Nano Lett.*, 2013, **13**, 2036-2040.
33. W. Tang, S. Tian, L. Liu, L. Li, H. Zhang, Y. Yue, Y. Bai, Y. Wu and K. Zhu, *Electrochem. Commun.*, 2011, **13**, 205-208.
34. R. Raccichini, A. Varzi, S. Passerini and B. Scrosati, *Nat. Mater.*, 2015, **14**, 271-279.
35. F. Bonaccorso, L. Colombo, G. Yu, M. Stoller, V. Tozzini, A. C. Ferrari, R. S. Ruoff and V. Pellegrini, *Science*, 2015, **347**, 1246501.
36. B. Li, X. Wei, Z. Chang, X. Chen, X.-Z. Yuan and H. Wang, *Mater. Lett.*, 2014, **135**, 75-78.
37. Z. Wu, X. Pu, X. Ji, Y. Zhu, M. Jing, Q. Chen and F. Jiao, *Electrochim. Acta*, 2015, **174**, 238-245.
38. X.-h. Xia, J.-p. Tu, Y.-j. Mai, X.-l. Wang, C.-d. Gu and X.-b. Zhao, *J. Mater. Chem.*, 2011, **21**, 9319-9325.
39. M. H. Alfaruqi, V. Mathew, J. Gim, S. Kim, J. Song, J. P. Baboo, S. H. Choi and J. Kim, *Chem. Mater.*, 2015.
40. K. Kushida and K. Kuriyama, *physica status solidi (c)*, 2015.

Figure caption

Scheme 1. Schematic illustration of the fabrication of the LMO-MSs@GNSs composites

Fig.1. shows the XRD patterns of the obtained GNSs, γ-MnO2, LMO, LMO-MSs and LMO-MSs@GNSs composites

Fig.2. the SEM images of the obtained (a-b) γ-MnO_2, (c-d) LMO-MSs, (e-f) LMO-MSs@GNSs composites and (g) LMO, (h) Energy Dispersive Spectrometer (EDS) of LMO-MSs@GNSs composites

Fig.3. TEM images of (a) LMO-MSs and (b) LMO-MSs@GNSs composites, HRTEM images of (c) LMO-MSs and (d) LMO-MSs@GNSs composites, (e) TEM image of the LMO-MSs@GNSs composites with corresponding elemental mapping images of C (Carbon), O (Oxygen), and Mn (manganese)

Fig.4. CV curves of LMO/AC, LMO-MSs/AC and LMO-MSs@GNSs/AC lithium-ion capacitors at 10 $mV \cdot s^{-1}$ in the voltage range of 0.0-2.3 V

Fig.5. GC curves of LMO/AC, LMO-MSs/AC and LMO-MSs@GNSs/AC lithium-ion capacitors at 2 C in the voltage range of 0.0-2.3 V

Fig.6. The rate performance of LMO/AC, LMO-MSs/AC and LMO-MSs@GNSs/AC lithium-ion capacitors

Fig.7. Energy density and power density of LMO/AC, LMO-MSs/AC and LMO-MSs@GNSs/AC lithium-ion capacitors at different current density

Fig. 8. Cyclic performance curves of LMO/AC, LMO-MSs/AC and LMO-MSs@GNSs/AC lithium-ion capacitors and the inset shows the micrographs of cycled LMO-MSs@GNSs electrodes

Tab.1. The content of Mn ions in the electrolyte for LMO/AC, LMO-MSs/AC and LMO-MSs@GNSs/AC lithium-ion capacitors

Fig.9. EIS curves of LMO/AC, LMO-MSs/AC and LMO-MSs@GNSs/AC lithium-ion capacitors. The inset shows the equivalent circuit to fit the EIS.

Scheme 1. Schematic illustration of the fabrication of the LMO-MSs@GNSs composites

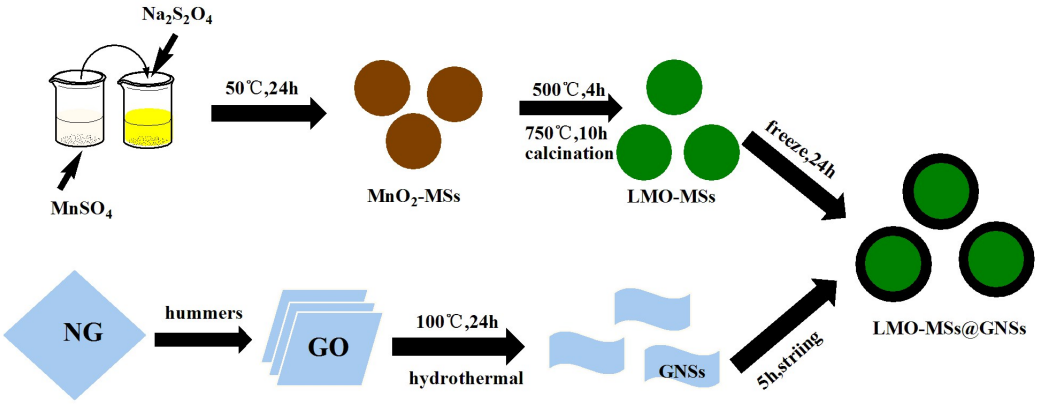

Scheme 1.

Fig.1. shows the XRD patterns of the obtained GNSs, γ-MnO_2, LMO, LMO-MSs and LMO-MSs@GNSs composites

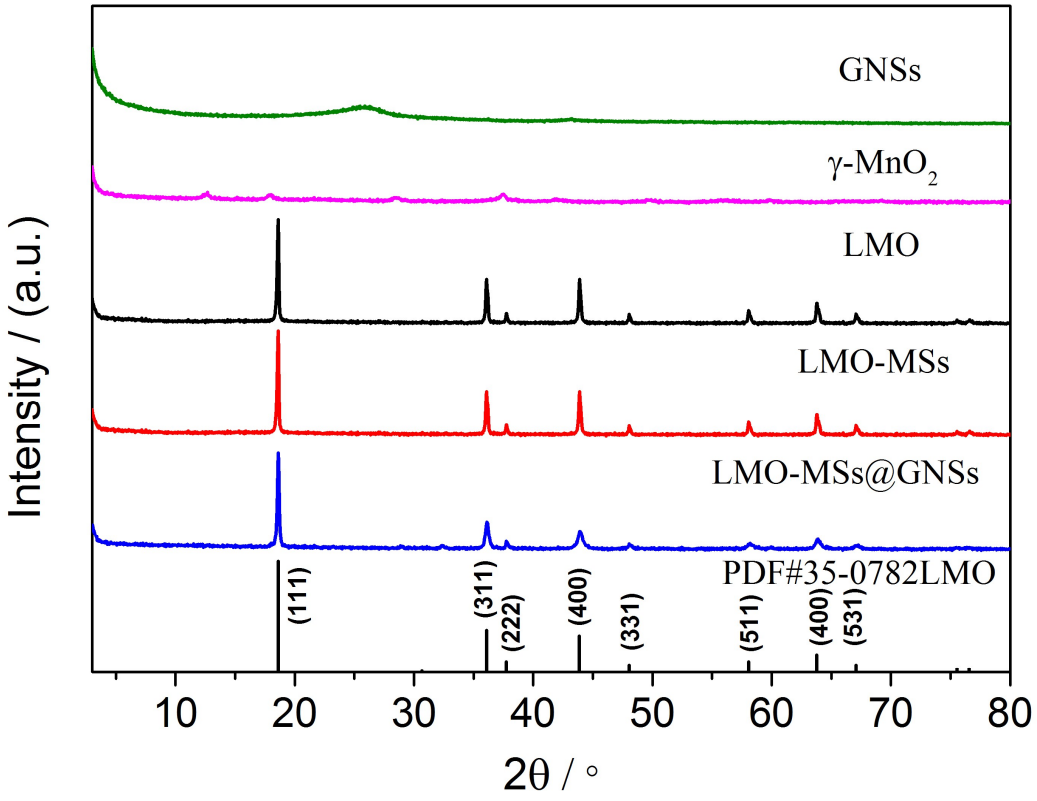

Fig.1.

Fig.2. the SEM images of the obtained (a-b) γ-MnO_2, (c-d) LMO-MSs, (e-f) LMO-MSs@GNSs composites and (g) LMO, (h) Energy Dispersive Spectrometer (EDS) of LMO-MSs@GNSs composites

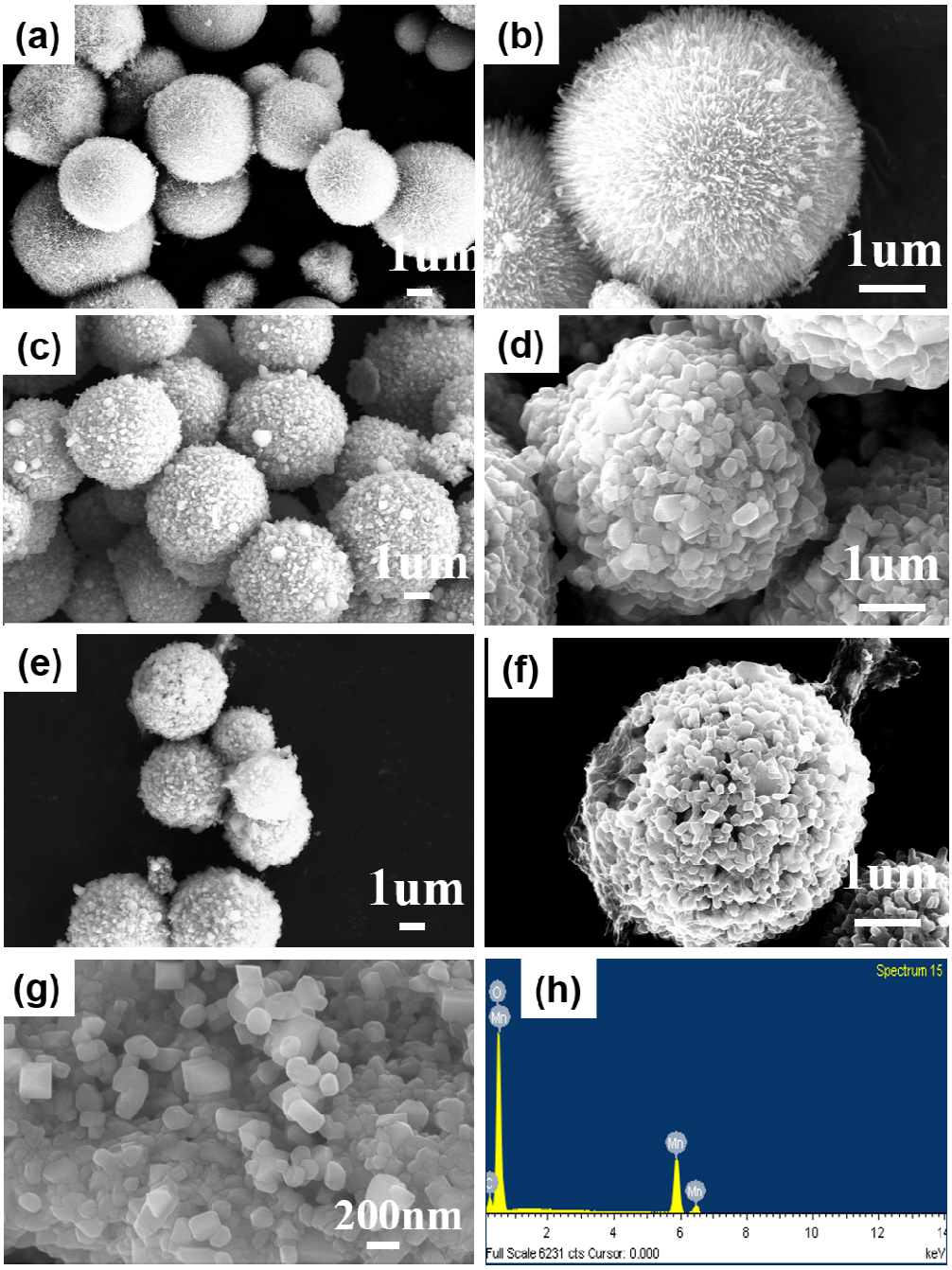

Fig.3. TEM images of (a) LMO-MSs and (b) LMO-MSs@GNSs composites, HRTEM images of (c) LMO-MSs and (d) LMO-MSs@GNSs composites, (e) TEM image of the LMO-MSs@GNSs composites with corresponding elemental mapping images of C (Carbon), O (Oxygen), and Mn (manganese)

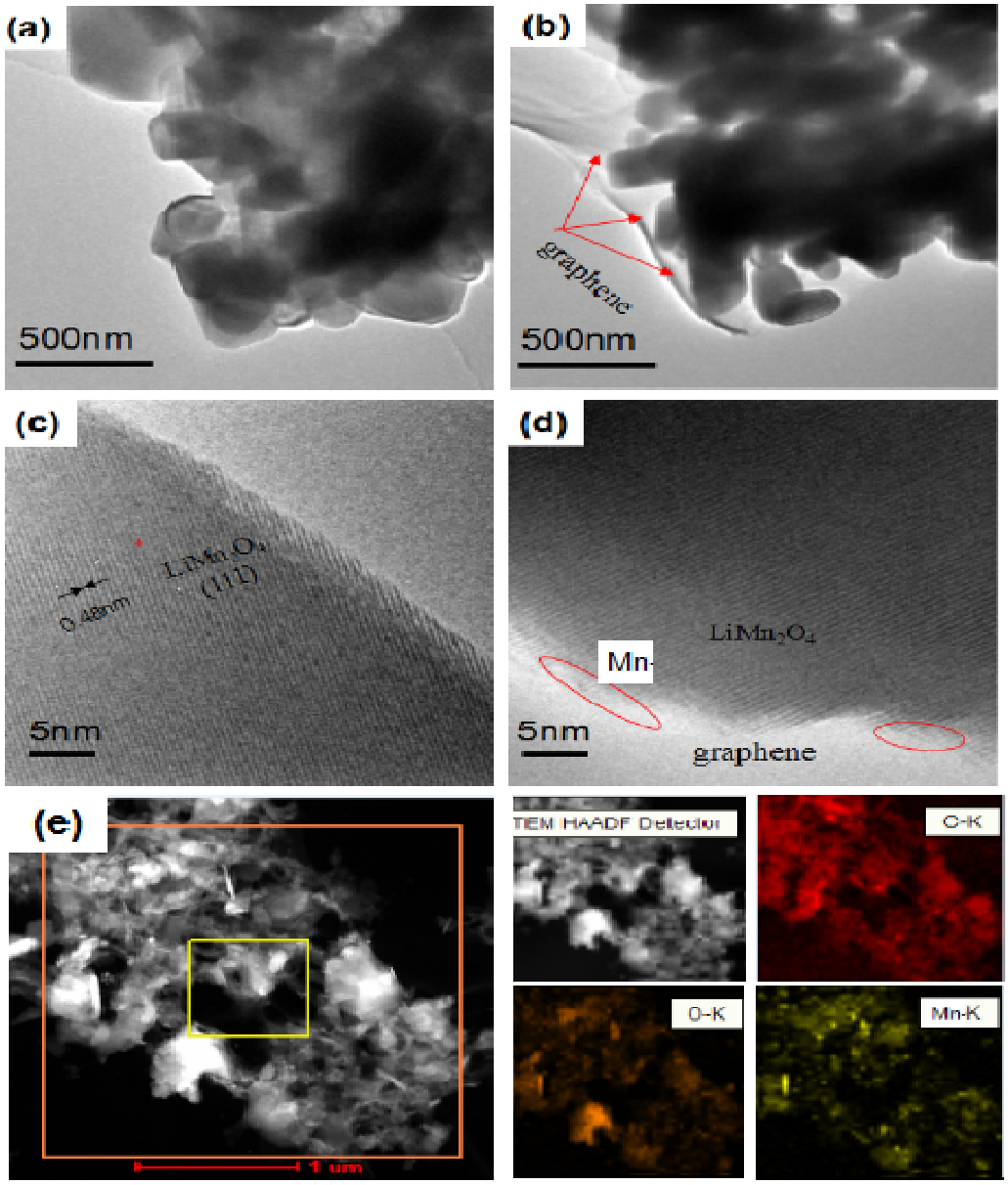

Fig.4. CV curves of LMO/AC, LMO-MSs/AC and LMO-MSs@GNSs/AC lithium-ion capacitors at 10 $mV \cdot s^{-1}$ in the voltage range of 0.0-2.3 V

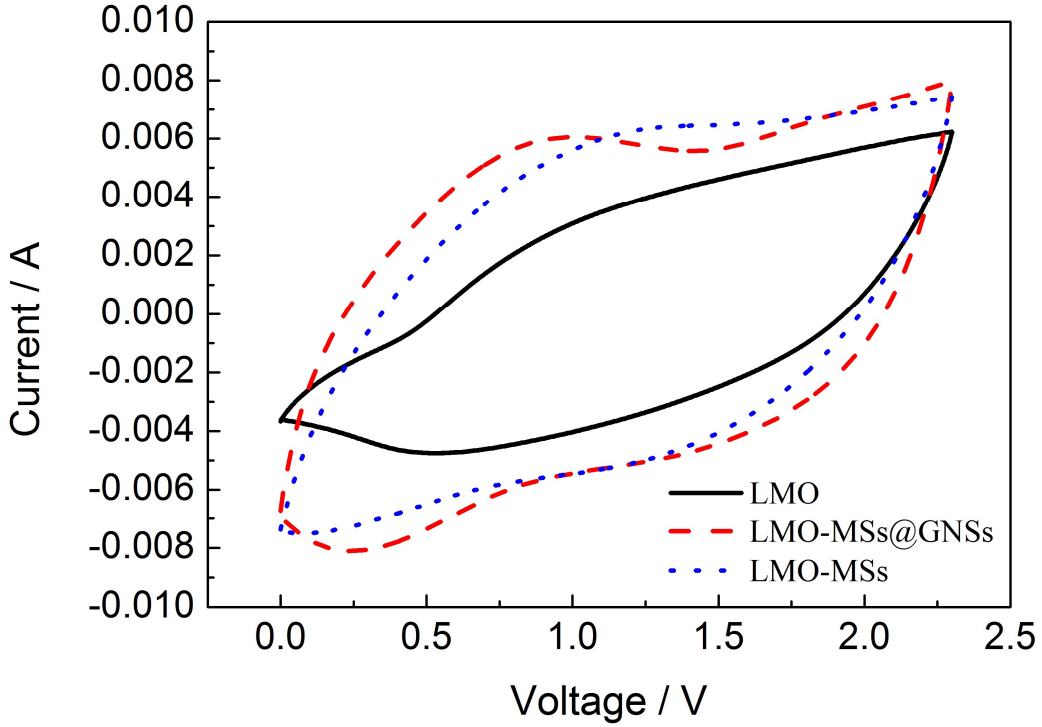

Fig.4.

Fig.5. GC curves of LMO/AC, LMO-MSs/AC and LMO-MSs@GNSs/AC lithium-ion capacitors at 2 C in the voltage range of 0.0-2.3 V

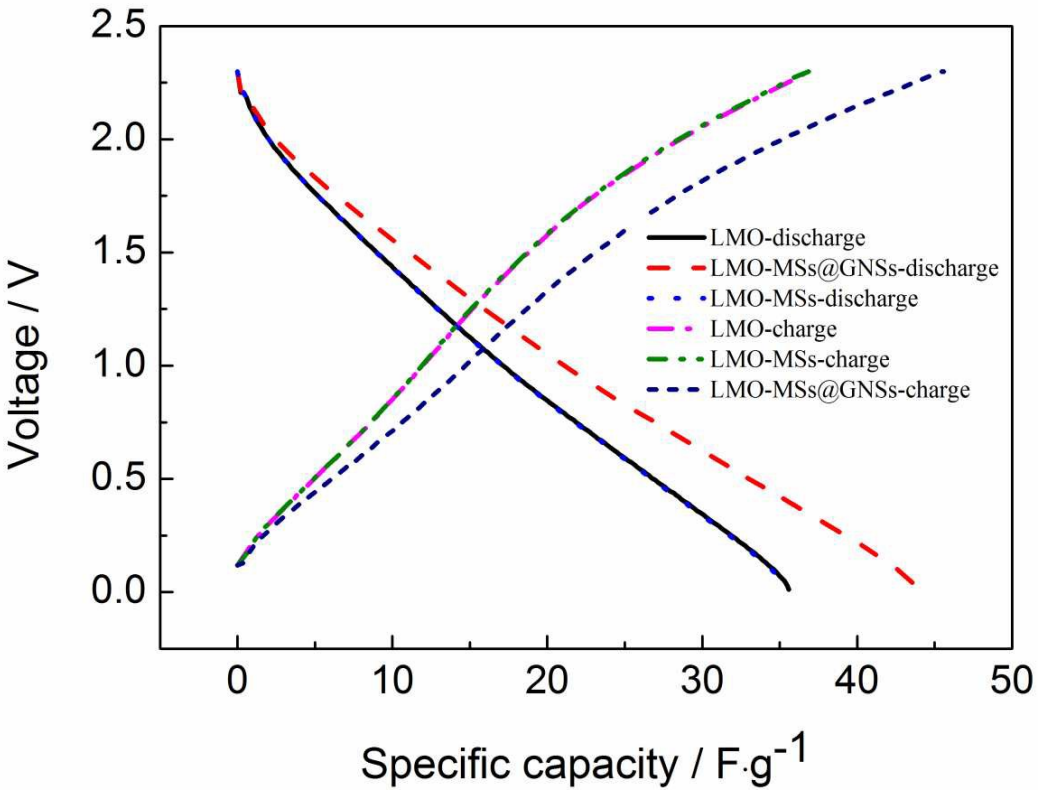

Fig.5.

Fig.6. The rate performance of LMO/AC, LMO-MSs/AC and LMO-MSs@GNSs/AC lithium-ion capacitors

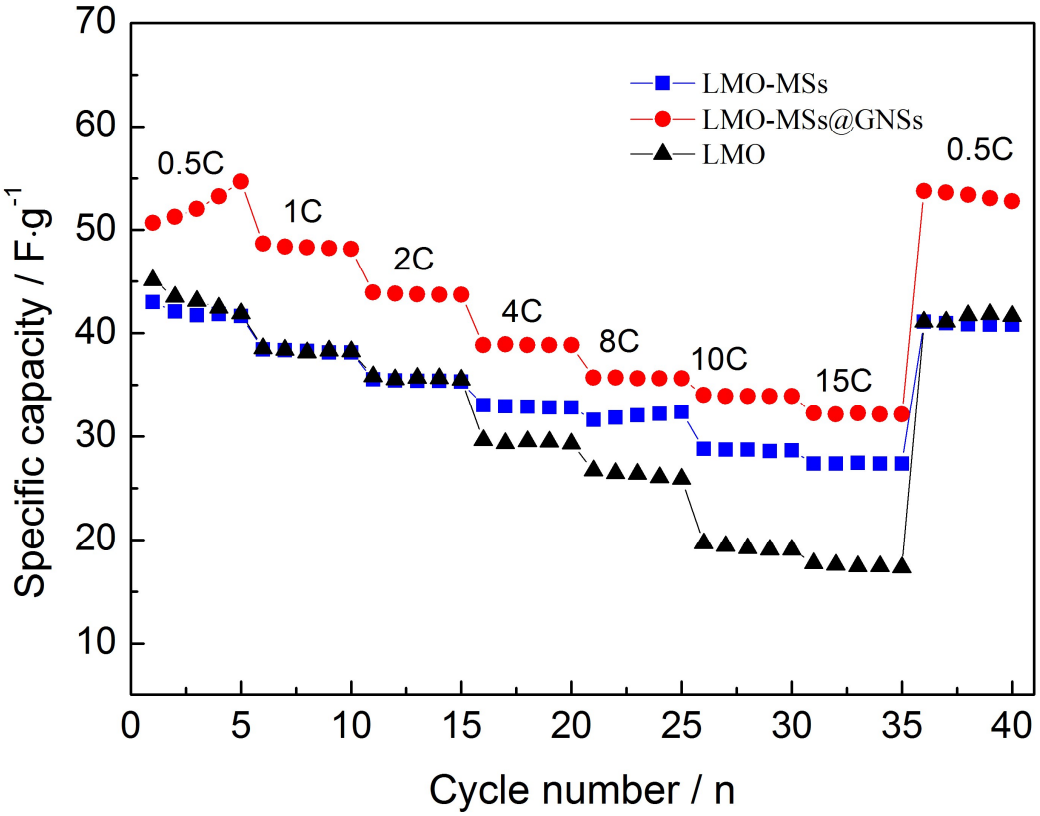

Fig.6.

Fig.7. Energy density and power density of LMO/AC, LMO-MSs/AC and LMO-MSs@GNSs/AC lithium-ion capacitors at different current density

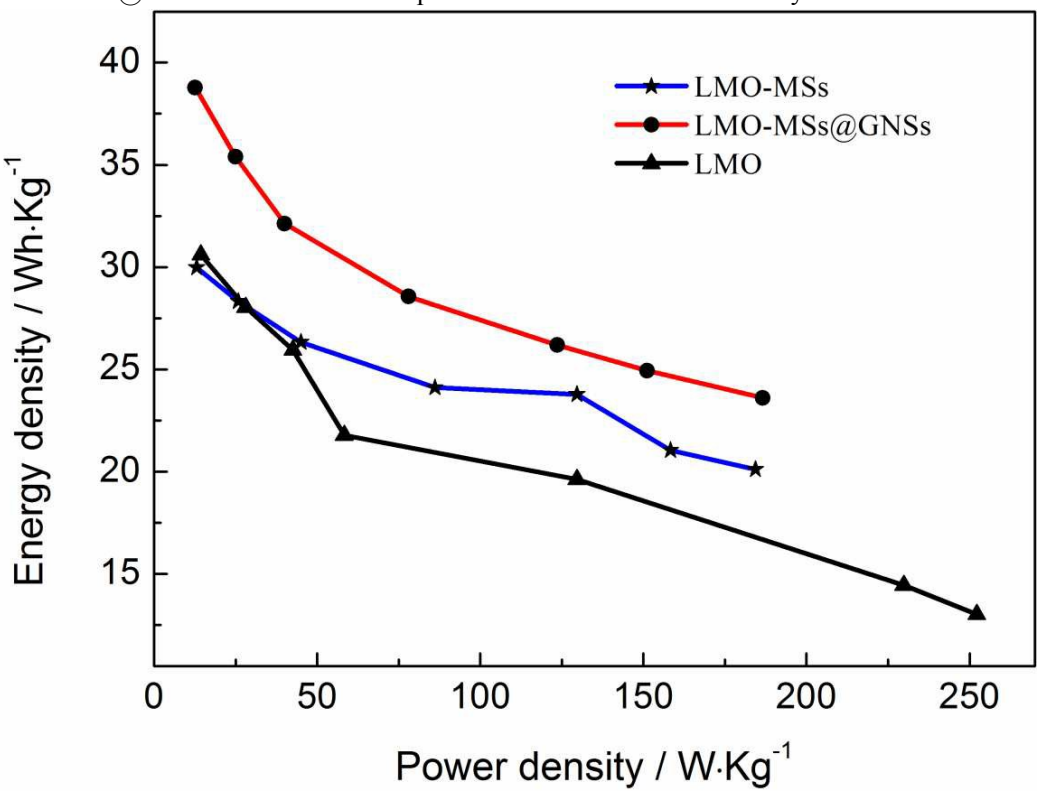

Fig.7.

Fig. 8. Cyclic performance curves of LMO/AC, LMO-MSs/AC and LMO-MSs@GNSs/AC lithium-ion capacitors and the inset shows the micrographs of cycled LMO-MSs@GNSs electrodes

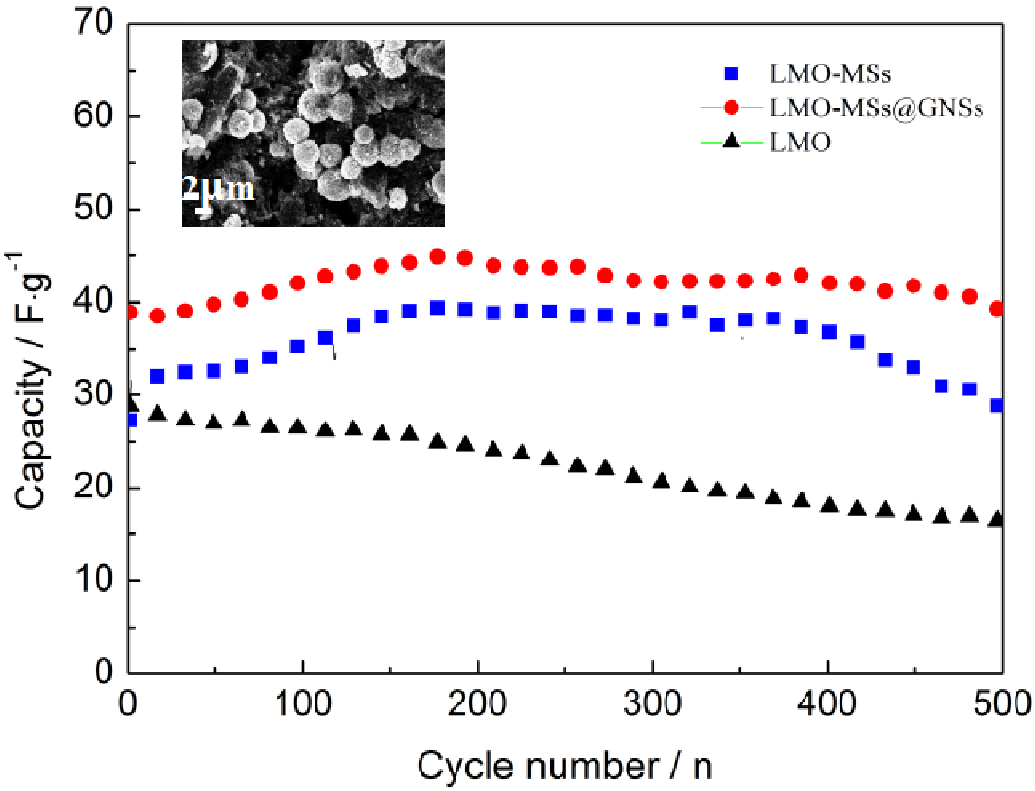

Fig.8.

Tab.1. The content of Mn ions in the electrolyte for LMO/AC, LMO-MSs/AC and LMO-MSs@GNSs/AC lithium-ion capacitors

Lithium-ion capacitors	Mn ($ug \cdot mL^{-1}$)
LMO/AC	1.555
LMO-MSs/AC	0.546
LMO-MSs@GNSs/AC	0.265

Tab.1.

Fig.9. EIS curves of LMO/AC, LMO-MSs/AC and LMO-MSs@GNSs/AC lithium-ion capacitors. The inset shows the equivalent circuit to fit the EIS.

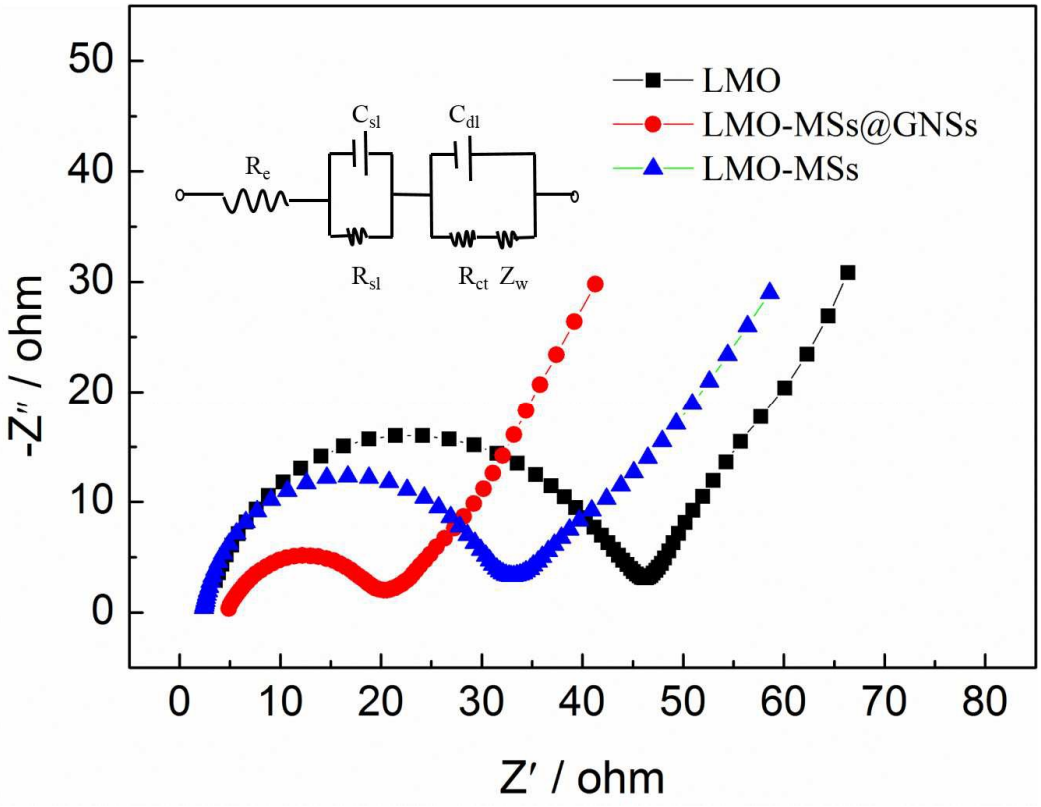

Fig.9.